Laser ablation reveals the impact of Cdc15p on the stiffness of the contractile ring

Mohamed Moshtohry[b,†], Kimberly Bellingham-Johnstun[a,†], Mary Williard Elting[b,c,*], and Caroline Laplante[a,c,*]

[a]Department of Molecular Biomedical Sciences, [b]Department of Physics, and [c]Cluster for Quantitative and Computational Developmental Biology, North Carolina State University, Raleigh, NC 27607

ABSTRACT **The mechanics that govern the constriction of the contractile ring remain poorly understood yet are critical to understanding the forces that drive cytokinesis. We used laser ablation in fission yeast cells to unravel these mechanics focusing on the role of Cdc15p as a putative anchoring protein. Our work shows that the severed constricting contractile ring recoils to a finite point leaving a gap that can heal if less than ~1 µm. Severed contractile rings in Cdc15p-depleted cells exhibit an exaggerated recoil, which suggests that the recoil is limited by the anchoring of the ring to the plasma membrane. Based on a physical model of the severed contractile ring, we propose that Cdc15p impacts the stiffness of the contractile ring more than the viscous drag.**

Monitoring Editor
Alex Mogilner
New York University

Received: Oct 25, 2021
Revised: Feb 22, 2022
Accepted: Feb 28, 2022

INTRODUCTION

The cytokinetic contractile ring generates forces that must be relayed to the plasma membrane by an anchoring mechanism. The anchoring mechanism is critical for cytokinesis yet how it impacts the mechanical properties of the contractile ring remains unknown. In fission yeast, the contractile ring assembles from the coalescence of nodes, cortical protein complexes containing the F-BAR domain protein Cdc15p, IQGAP homolog Rng2p, the formin Cdc12p, and the myosin-II molecule Myo2 (composed of the Myo2p heavy chain and Rlc1p and Cdc4p light chains) through the search-capture-pull-release mechanism (SCPR) (Wu *et al.*, 2003; Wu *et al.*, 2006; Vavylonis *et al.*, 2008). In the constricting contractile ring, the core of the node, including Cdc15p and the tips of Myo2 tails, localizes at the plasma membrane while the Myo2 heads, the bundle of actin filaments and myosin-II Myp2 molecules are located ~60 nm away from the membrane (Laplante *et al.*, 2016; McDonald *et al.*, 2017; Swulius *et al.*, 2018). The molecular composition and organization of nodes suggest that they may anchor the bundle of actin filaments to the membrane (Laplante *et al.*, 2016; Bellingham-Johnstun *et al.*, 2021).

Anchoring the contractile ring to the plasma membrane and cell wall likely requires a complex mechanism involving distinct proteins including but not limited to the F-BAR containing proteins Cdc15p, Rga7p and Imp2p and the beta-glucan synthase Bgs1p (Arasada and Pollard, 2014, 2015; McDonald *et al.*, 2015; Snider *et al.*, 2017; Willet *et al.*, 2021). Cdc15p contains an F-BAR domain at its N-terminus, a ~600 amino acids disordered region followed by a SH3 domain at its C-terminus. Multiple lines of evidence suggest that Cdc15p anchors the contractile ring to the plasma membrane and septum. First, mutation and deletion of *cdc15* and depletion of the protein Cdc15p result in sliding of the contractile ring (Arasada and Pollard, 2014; McDonald *et al.*, 2015). Second, Cdc15p interacts with the plasma membrane at its F-BAR domain and with actin filaments indirectly by binding to other node components Cdc12p and Rng2p (Carnahan and Gould, 2003; Tebbs and Pollard, 2013; McDonald *et al.*, 2015; Willet *et al.*, 2018). Finally, Cdc15p supports the timely transport of the septum producing enzyme Bgs1p, another candidate anchor protein, from the Golgi to the plasma membrane. In cells depleted of Cdc15p, contractile ring sliding ends when a critical number of Bgs1p-mEGFP molecules reach the division plane, suggesting that Bgs1p is the main anchor that prevents

This article was published online ahead of print in MBoC in Press (http://www.molbiolcell.org/cgi/doi/10.1091/mbc.E21-10-0515) on March 11, 2022.

†These authors contributed equally.

Author contributions: conceptualization, data curation and analysis (Supplemental Figure 2, A and D), building physical model and diagrams, writing the manuscript, building figures, and funding: C.L.; conceptualization, physical model and equations, laser ablation method, and manuscript editing: M.W.E.; initial ablation troubleshooting, data collection and analysis (Figures 1, A and B, and 3A; Supplemental Figures 1E, 2B, and 4), and coding: M.M.; conceptualization, data collection and analysis (Figures 1, C and D, and 3, B–F; and Supplemental Figures 1, B and C and 2, E and F, and 3, A and C), coding, manuscript writing and editing, and molecular and cellular biology: K.B.J.

*Addresses correspondence to: Caroline Laplante (claplan@ncsu.edu); Mary Williard Elting (mary.elting@ncsu.edu).

Abbreviations used: F-BAR, Fes/CIP4 homology Bin-Amphiphysin-Rvs; IQGAP, isoleucine-glutamine GTPAse activating protein; SH3, Src homology 3.

the sliding of the contractile ring (Arasada and Pollard, 2014). Therefore, Cdc15p may have dual anchoring roles by linking the actin bundle to the plasma membrane and influencing septum deposition. These putative anchoring roles may be conserved as F-BAR domain containing proteins involved in modulating the actin cytoskeleton and in cytokinesis are conserved in budding yeast (HOF1) and in higher eukaryotes (proline, serine, threonine phosphatase interacting protein, PSTPIP) (Spencer *et al.*, 1997; Angers-Loustau *et al.*, 1999; Oh *et al.*, 2013).

Here, we used laser ablation in fission yeast to determine the mechanical role of Cdc15p during cytokinesis. Laser ablation degrades cellular structures in a diffraction-limited spot via photodamage using a focused pulsed laser and can reveal the mechanics of actin contractile structures (Kumar *et al.*, 2006; Colombelli *et al.*, 2009; Russell *et al.*, 2009; Silva *et al.*, 2016; Wollrab *et al.*, 2016; Kassianidou *et al.*, 2017; Spira *et al.*, 2017). Constricting contractile rings in fission yeast recoil after being severed, revealing a gap of finite size that can heal is less than ~1 μm. The recoil profile of ablated contractile rings suggests that the contractile ring is a viscoelastic material under tension. Ablated contractile rings in Cdc15p-depleted cells exhibit greater and slower recoil with defective healing compared with wild type. Our measurements combined with mechanical model of the contractile ring show that the loss of Cdc15p results in decreased stiffness of the contractile ring material.

RESULTS AND DISCUSSION

Using laser ablation, we severed the contractile rings of wild-type fission yeast cells expressing mEGFP-Myp2p to highlight the bundle of actin filaments of the ring (Laplante *et al.*, 2015). We imaged each cell prior to laser ablation, ablated a portion of its contractile ring, and then imaged the response every second for up to ~5 min unless the fluorescent signal from mEGFP-Myp2p was photobleached or the sample was lost due to a drift in the z-position (see *Materials and Methods*). We acquired time-lapse images of a single optical plane of the surface of the contractile ring to maximize temporal resolution and reduce photodamage (Supplemental Figure 1A). We focused on constricting contractile rings (~75% of their initial size corresponding to 8–9 μm in circumference) to avoid potentially confounding results from contractile rings that have not yet started to constrict as they may have distinct mechanical properties. In response to laser ablation, we observed a mechanical recoil response that suggested the contractile ring was completely severed, rather than partially cut (Figure 1A). In contrast, when targeting the plasma membrane of cells expressing the plasma membrane marker Rho2^{CAAX}-HALO and stained with HALO-JF635, we observed a marked decrease in cell volume likely caused by damage to both the plasma membrane and the cell wall (Figure 1B) (Atilgan *et al.*, 2015). This different response suggests that when we sever the contractile ring, the integrity of the cell wall and the plasma membrane is maintained. Thus, we interpret the recoil response of the contractile ring to laser ablation as a specific readout of its mechanics.

To determine if severed contractile rings continue to constrict while the ring is discontinuous, we performed serial ablations on the same contractile ring and calculated ring circumference before and after the series of ablations. We re-ablated severed contractile rings just before they fully healed from their previous cut to maintain their discontinuity (Figure 1C). We used uncut cells neighboring the cells severed by laser ablation as controls. Rings treated by serial ablations constricted at a rate of 0.15 ± 0.05 μm (mean ± SD, $n = 6$) compared to 0.28 ± 0.11 μm ($n = 8$) for rings that were not ablated. Therefore, discontinuous contractile rings constrict as observed in *Caenorhabditis elegans* (Silva *et al.*, 2016), suggesting that the ring fragment maintains tension away from the cut site. The reduction in constriction rate may be caused by imperceptible damages to the cells, or the gap in the severed rings may slow their overall constriction even though tension is maintained in the remaining ring fragment.

Immediately following ablation, the tips of the severed contractile ring (severed tips) recoiled away from each other revealing a growing gap (Figure 1A) (Silva *et al.*, 2016). We interpret the recoil as a release of the tension that was present in the ring prior to ablation (Kumar *et al.*, 2006; Silva *et al.*, 2016; Kassianidou *et al.*, 2017). The recoil phase lasted 33 ± 25 s (mean ± SD, $n = 23$ severed tips). The severed tips then stopped recoiling and the newly formed gap in the severed contractile ring closed in an apparent healing phase, comparable to what has been observed in *C. elegans* (Silva *et al.*, 2016). The duration of the healing phase was 63 ± 46 s (mean ± SD, $n = 10$ cells) (Supplemental Figure 1B). Approximately 80% of severed wild-type contractile rings healed completely by the end of the 5 min acquisition (Supplemental Figure 1C). During the healing phase, the two severed tips progressively approached each other, remaining mostly aligned with the plane of the ring, suggesting the presence of a mechanism that limits the lateral movement of the ring material. In the cells that failed to heal the severed contractile ring, the severed tips remained static after the end of the recoil suggesting that if severed tips initiate healing, they heal to completion. Although the reason for the failure in healing was unknown, these cells recoiled to reveal a slightly larger gap than average (Supplemental Figure 1C), suggesting that larger gaps may be more difficult to heal. The healing of severed contractile rings suggests that it is a self-healing material or supports the presence of a mechanism that can detect and repair damage and ensure robust cytokinesis. The molecular mechanism that governs the healing remains unknown. However, the connection of severed tips is reminiscent of the response observed when two adjacent contractile rings connect and eventually zip into a single ring (Daga and Chang, 2005). Zippering of neighboring rings can be recapitulated in simulations of the SCPR mechanism, where actin filaments polymerized by Cdc12p in the nodes of one contractile ring are captured and pulled by Myo2 in the nodes of a neighboring contractile ring (Vavylonis *et al.*, 2008). Similarly, the SCPR mechanism may drive the healing of severed contractile ring tips, with actin filaments polymerized and captured by Myo2 in nodes positioned across the gap caused by laser ablation (Supplemental Figure 1D). A similar healing ability is also observed in severed contractile rings in *C. elegans* and in stress fibers suggesting that the ability to heal may be conserved (Kumar *et al.*, 2006; Silva *et al.*, 2016).

We tracked the position of the severed tips at each time frame and calculated the displacement of each severed tip over time as the distance from its initial position immediately after the cut. While we were able to visualize both severed tips in a few severed contractile rings, only one tip remained in our observation plane in most cases (Supplemental Figure 1A). The displacements of the severed tips during the recoil phase followed an exponential profile (Figure 1D and Supplemental Figure 1E). An exponential recoil is often observed in response to the ablation of sub-cellular structures and can be used to infer the viscoelastic properties of the ablated material (Kumar *et al.*, 2006; Colombelli *et al.*, 2009; Silva *et al.*, 2016; Roca-Cusachs *et al.*, 2017). We averaged the displacement of the recoil phase (hereby referred to as the displacement) of 26 severed tips of wild-type contractile rings to find the mean response to ablation during an 80 s period (Figure 1D). The mean displacement of the severed tips during recoil ΔL fits to a single exponential,

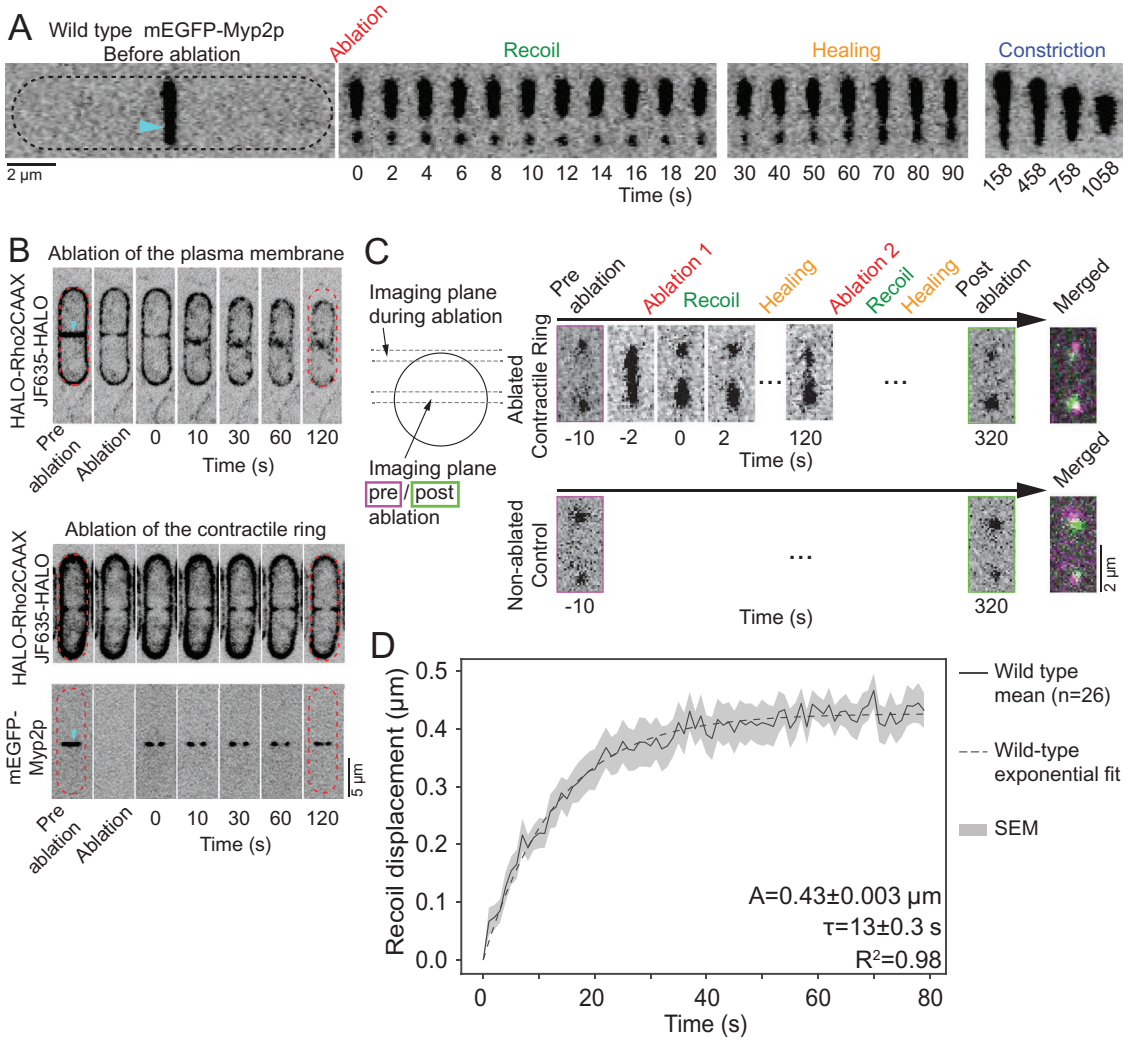

FIGURE 1: Ablated contractile rings in wild-type cells exhibit recoil followed by healing and constriction. (A) Left, single plane spinning disk confocal micrograph of a representative wild-type cell (dashed line outlines the cell) expressing mEGFP-Myp2p to visualize the contractile ring before ablation (targeted at cyan arrowhead). Right, cropped frames showing phases of the response to ablation. (B) Single plane confocal micrographs taken at the center of cells showing the cell shape following laser ablation. Plasma membrane is labeled with JF635-HALO bound to HALO-Rho2^{CAAX}. Top, cell size decreases when the plasma membrane is targeted by laser ablation. Bottom, cell size remains constant when the contractile ring is targeted by laser ablation. Laser ablation targeted at cyan arrowheads. Dashed red line outlines the cells before ablation. (C) Left, diagram showing the two imaging planes used in this panel. Top right, time lapse micrographs of serial ablation of contractile ring. Image of ring diameter before (purple) and after ablation (green) were merged to show the size difference. Bottom right, micrographs of ring diameter of a neighboring non-ablated control cell taken at the same timepoint as the before ablation (purple), and after ablation (green). Merged image shows the size difference. (D) Mean recoil displacement (solid line) ± standard error of the mean of all traces (SEM, shaded region) of 26 severed tips of ablated wild-type contractile rings. Exponential fit (dotted line) to this mean trace and its fit parameters (± the standard error on the least squares fit parameters) are listed. Time 0, first frame after ablation. Fluorescence, inverted grayscale, except for merged images.

$\Delta L(t) = A\left(1 - e^{-\frac{t}{\tau}}\right)$, where the total magnitude of the recoil after ablation, A = 0.43 ± 0.003 µm (mean ± standard error on the least squares fit, SE, n = 26), and the timescale of viscoelastic recoil, τ = 13 ± 0.3 s (mean ± SE). The relatively small magnitude of the recoil from one severed tip, corresponding to total gap size of ~0.9 µm assuming equal recoil from both tips (~10% of the 8–9 µm ring circumference), can be explained by the presence of an anchoring mechanism that limits the extent to which the initial tension in the ring can be released during recoil.

We schematically represented the severed tips of the contractile rings as springs and dashpots (Kelvin-Voigt elements) in parallel, anchored to a fixed boundary, the plasma membrane and cell wall (Figure 2A). The "bonds" that anchor the ring can turnover or rupture to allow the ring to slide but ultimately bear the load of the tension. The spring represents the overall effective stiffness k_{eff} determined by the sum of the elastic forces. The dashpot represents the overall effective viscous drag η_{eff} determined by the sum of the viscous drag of the contractile ring material and surrounding medium. We expect that all components of the contractile ring, including the contractile bundle of actin filaments and the anchoring

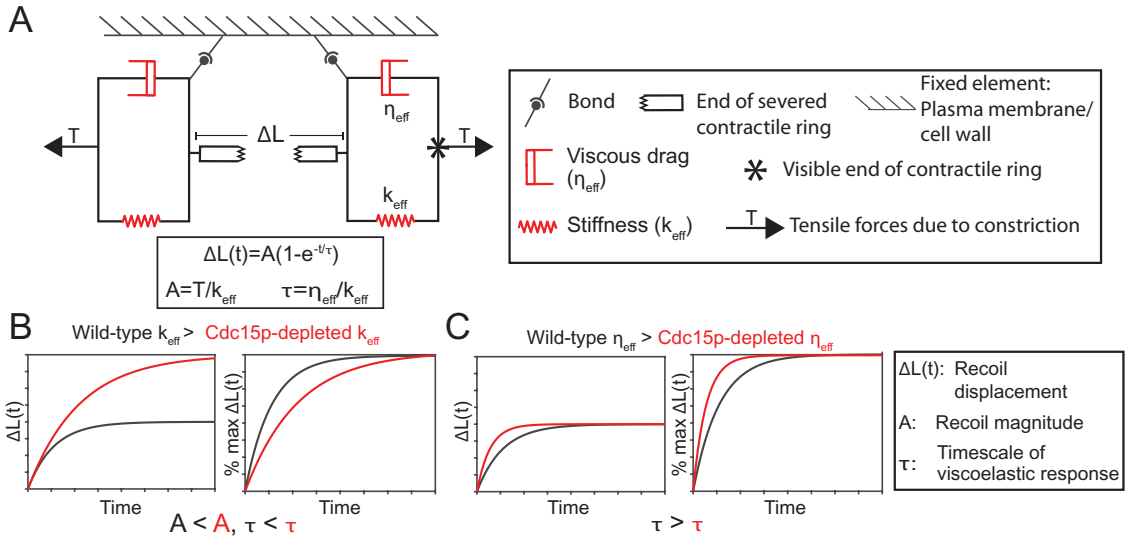

FIGURE 2: Severed contractile ring recoil behavior supports a viscoelastic force model. (A) Model of the viscoelastic forces governing the behavior of the release of tension of the contractile ring after ablation. (B, C) Graphs of simulated data for the predicted outcomes of ablating contractile rings depleted for Cdc15p. Right, these simulated recoil displacement data are rescaled as a percentage of the maximum displacement to visualize the effect of changing τ. (B) Predicted graphs of recoil displacement versus time (left) and percent of max displacement versus time (right) if the effective stiffness k_{eff} is reduced in Cdc15p-depleted cells. If Cdc15p-depletion reduces k_{eff} (without changing η_{eff}), the result would be an increased amplitude A and timescale τ compared with wild type. (C) Predicted graphs of displacement versus time (left) and percent of max displacement versus time (right) if the effective viscous drag η_{eff} is reduced in Cdc15p-depleted cells. If Cdc15p-depletion reduces η_{eff} (without changing k_{eff}), the result would be reduced timescale τ and unchanged amplitude A compared with wild type.

components, contribute to k_{eff} and η_{eff}. We assume that, prior to the cut, the contractile ring is under tension T_0 (McDargh *et al.*, 2021). The sources of this tension include both contractile forces from myosin binding to and sliding actin filaments and elastic forces anchoring the ring to the plasma membrane and cell wall that distribute the load of T_0 around the cell periphery. After the cut, we assume T_0 is locally released while the ring maintains its tension far from the cut site. During the local release of T_0 in response to severing, the profile of recoil is determined by the sum of all elastic and viscous forces in the ring (Supplemental Text). Using this framework, the recoil magnitude *A* is given by the ratio of the tension before the cut and the effective stiffness of the ring $A = T_0/k_{eff}$. The timescale of the viscoelastic recoil τ is given by the ratio of the effective viscous drag to the effective stiffness of the ring $\tau = \eta_{eff}/k_{eff}$. Thus, *A* and τ describe the displacement profile and are both influenced by the mechanical properties of the contractile ring, including its anchoring to the plasma membrane and cell wall.

This framework predicts that changing the properties of the contractile ring would alter its response to ablation. As anchoring forces oppose the forces that make the ring constrict, effectively stiffening the ring, we expected that weakening the anchoring would decrease k_{eff} and result in a greater recoil magnitude *A* (Figure 2B). Additionally, we expected that weakening the anchoring may reduce η_{eff} by weakening the connections to the plasma membrane and cell wall. The relationship between k_{eff}, η_{eff} and τ made predicting the change in τ more difficult since a reduction in k_{eff} without a change in η_{eff} would result in a higher τ (Figure 2B), while a reduction in η_{eff} without a change in k_{eff} would result in a lower τ (Figure 2C).

We depleted Cdc15p to determine its impact on the mechanics of the contractile ring. We measured the extent of depletion by comparing the level of fluorescence of the repressed mEGFP-Cdc15p construct to the same construct expressed under the control of the *cdc15* endogenous promoter. Under repressed conditions, the mEGFP-Cdc15p construct is expressed at ~3% of endogenous levels (Supplemental Figure 2A). Under derepressed conditions, the construct is expressed at ~25% of endogenous levels. For ablation, we depleted mCherry-Cdc15p in cells expressing mEGFP-Myp2p. As expected from our experiment with mEGFP-Cdc15p, most cells depleted of Cdc15p did not accumulate any detectable mCherry-Cdc15p in their contractile rings (Supplemental Figure 2B). In about half of Cdc15p-depleted cells, contractile rings assembled at the cell center but slid off center before the onset of constriction resulting in septum offset as previously observed (Supplemental Figure 2, C and D) (Arasada and Pollard, 2014; McDonald *et al.*, 2015). Cells depleted of Cdc15p constricted their contractile ring at ~0.2 μm/min, ~60% of the wild-type rate (Supplemental Figure 2, E and F).

We severed contractile rings of Cdc15p-depleted cells by laser ablation and tracked the position of the severed tips over time (Figure 3A and Supplemental Figure 3A). Like wild-type rings, ablated rings of Cdc15p-depleted cells recoiled albeit with a different displacement profile (Figure 3B and Supplemental Figure 3B). The recoil magnitude of the severed tips *A* approximately doubles ($A = 0.75 \pm 0.013$ μm, mean ± SE, $n = 26$) while the timescale τ of severed contractile rings nearly triples in Cdc15p-depleted cells ($\tau = 30 \pm 1.2$ s, mean ± SE) compared with wild-type cells (Figure 3, B and C). The experimental displacement curve for Cdc15p-depleted cells does not reach a plateau under our experimental conditions, likely because the severed tips recoil out of the imaging plane (Supplemental Figure 1A). Therefore, our reported values of *A* and τ represent lower limits on these responses.

Two lines of evidence suggests that T_0 decreases in Cdc15p-depleted cells, potentially due to weakened anchoring (Supplemental Text). First, we measured a reduction in constriction rate in Cdc15p-depleted cells (Supplemental Figure 2, E and F). Second,

McDargh *et al*. measured a ~60% decrease in the tension of contractile rings of fission yeast protoplasts expressing Myo2p-E1, a mutant version of Myo2p that binds poorly to actin filaments (Lord and Pollard, 2004; McDargh *et al.*, 2021). Based on the molecular organization of cytokinesis nodes, decreasing the interaction of Myo2p with actin filaments and depleting Cdc15p may cause a similar decrease in T_0. To understand the cause of the decrease in T_0, we measured the number of myosin molecules Myo2 and Myp2, the IQGAP Rng2p and the formin Cdc12p. We measured a decrease in Cdc12p in the contractile ring of ~40% of the cells, as reported previously, and a small albeit significant decrease in Rng2p, a protein involved in contractile ring assembly and stability (Figure 3D) (Laporte *et al.*, 2011; Tebbs and Pollard, 2013; Morita *et al.*, 2021). A decrease in Cdc12p may cause a decrease in the total number of actin molecules in the contractile ring leading to a lower T_0. We used *Pcof1-megfp-lifeact* to measure the total number of actin molecules in contractile rings (Malla *et al.*, 2021). We focused on contractile rings that had constricted to 80-50% of their initial size, like the ones targeted for ablation. We found no significant difference in the total number of actin molecules between wild-type and Cdc15p-depeleted cells (Figure 3E), suggesting that another formin such as For3p may be compensating for reduced Cdc12p or that the amount of actin in the ring does not scale perfectly with the amount of Cdc12p in the ring. We also measured comparable numbers of Myp2p or Myo2p proteins between wild-type and Cdc15p-depleted cells. Therefore, our results suggest that the decrease in tension is not caused by a reduction in actin or myosin motors in the contractile ring. Given the relationship $A = T_0/k_{\text{eff}}$, the increased A, and the likelihood that T_0 is decreased in the contractile rings of cells depleted of Cdc15p, our data suggests that the effective stiffness k_{eff} decreases in Cdc15p-depleted cells. Our data also support that Cdc15p and the anchoring mechanism function to bear the load exerted by the constriction of the contractile ring, thus contributing to its stiffness. As A and τ increased by a similar factor and the calculation of both A and τ rely on k_{eff}, depleting Cdc15p likely impacts k_{eff} more than η_{eff}. The marginal impact of depleting Cdc15p, a putative protein anchor, on η_{eff} may seem counterintuitive. However, there are an abundance of molecular interactions between proteins of the contractile ring and between the proteins of the contractile ring and cytoplasm, all of which may contribute to viscous drag. Therefore, depleting Cdc15p may only cause a marginal change in η_{eff}. Finally, we would expect a severe reduction in η_{eff} to result in faster constriction, as observed in contractile rings isolated from fission yeast ghosts (Mishra *et al.*, 2013; Wang and O'Shaughnessy, 2019). We instead measured a reduction in the constriction rate in Cdc15p-depleted cells suggesting that the ring tension and stiffness are still opposed by a considerable amount of viscous drag in these cells.

The severed contractile rings in cells depleted of Cdc15p rarely heal. The Cdc15p-depleted cells that healed had a smaller gap size at the end of the recoil (Figure 3F). The likelihood that a severed ring heals plummets when the gap size exceeds ~1.0 µm (corresponding to twice an A value of ~0.5 µm and assuming equal recoil from both severed tips). This suggests that the healing mechanism in fission yeast is competent to fix small discontinuities in the contractile ring but not larger gaps. The SCPR mechanism of contractile ring assembly provides a simple mechanism for healing limited by the size of the gap opened by severing (Vavylonis *et al.*, 2008). As Cdc15p contributes to anchoring, the healing ability of contractile rings may be indirectly linked to the anchoring mechanism.

Severing the contractile ring may result in the rearrangement of its protein components to meet the new mechanical constraints. To test this possibility, we examined the distribution of mEGFP-Myp2p before and after ablation. In uncut wild-type cells, mEGFP-Myp2p distributes unevenly around the contractile ring (Supplemental Figure 4B). The fluorescence intensity of mEGFP-Myp2p is often brightest at the edges of the visible portion of the contractile ring in our single plane confocal micrographs likely due to the curvature of the contractile ring (Supplemental Figure 1A). Shortly after severing, the intensity of mEGFP-Myp2p became brighter in the severed tip, ahead of the recoil motion (Supplemental Figure 4C). We measured the intensity of the brightest pixel (maximum fluorescence intensity) at each time point for the first 80 s after ablation. In severed wild-type and Cdc15p-depleted contractile rings, the maximum fluorescence intensity increased shortly after ablation (~15 s) and eventually decayed over time likely as the severed tip recoiled out of the imaging plane (Supplemental Figure 4, C and D). In contrast, the maximum fluorescence intensity of unsevered control contractile rings does not increase over 80 s (Supplemental Figure 4F) suggesting that mechanical perturbation of the contractile ring causes the increase in fluorescence intensity. To determine if this response is caused by the recruitment of protein from the cytoplasmic pool or by the re-distribution of existing mEGFP-Myp2p in the contractile ring upon severing, we measured the total fluorescence of the ring within the imaging plane over time. In intact contractile rings of wild-type and Cdc15p-depleted cells, the total integrated fluorescence remains roughly constant over time while in ablated contractile rings this value steadily decreased over time, likely due to partial retraction of the ring out of the imaging plane. (Supplemental Figure 4E). This decrease was more pronounced in Cdc15p-depleted cells, presumably since they undergo a greater recoil than the wild-type cells. Therefore, the increase in the maximum fluorescence intensity is likely due to the local concentration of mEGFP-Myp2p molecules already present in the ring rather than recruitment of new molecules.

Our work shows that the constricting contractile ring of fission yeast recoils to a finite point after being cut by laser ablation leaving a gap that can heal if less than ~1.0 µm. This recoil response suggests that tension present in the constricting contractile ring prior to ablation locally redistributes on laser cutting while the remaining ring fragment maintains tension. The anchoring mechanism of the contractile ring is likely responsible for locally isolating the redistribution of this load and thus maintaining the shape and mechanical integrity of the overall ring. The recoil profile of severed contractile rings in Cdc15p-depleted cells as well as the strong possibility of reduced tension in those rings suggest that Cdc15p impacts the stiffness k_{eff} more than the viscous drag η_{eff}.

As Cdc15p is a node component, our results suggest that nodes function, in part, as anchors that link the actin bundle to the plasma membrane. The molecular composition and organization of the nodes support a role in linking the bundle of actin filaments to the plasma membrane through the actions of Myo2, Rng2p, Cdc12p and Cdc15p. However, the anchoring mechanism likely requires connections to the cell wall as well as to the plasma membrane. Arasada and Pollard proposed that the anchoring function of Cdc15p is due, at least in part, to its role in trafficking the septum producing enzyme Bgs1p to the cell surface at the division plane (Arasada and Pollard, 2014). Therefore, the contributions of the plasma membrane and cell wall to the overall anchoring mechanism are likely interconnected, and some aspects of the role of Cdc15p in anchoring may be indirect.

METHODS AND MATERIALS

Request a protocol through *Bio-protocol*.

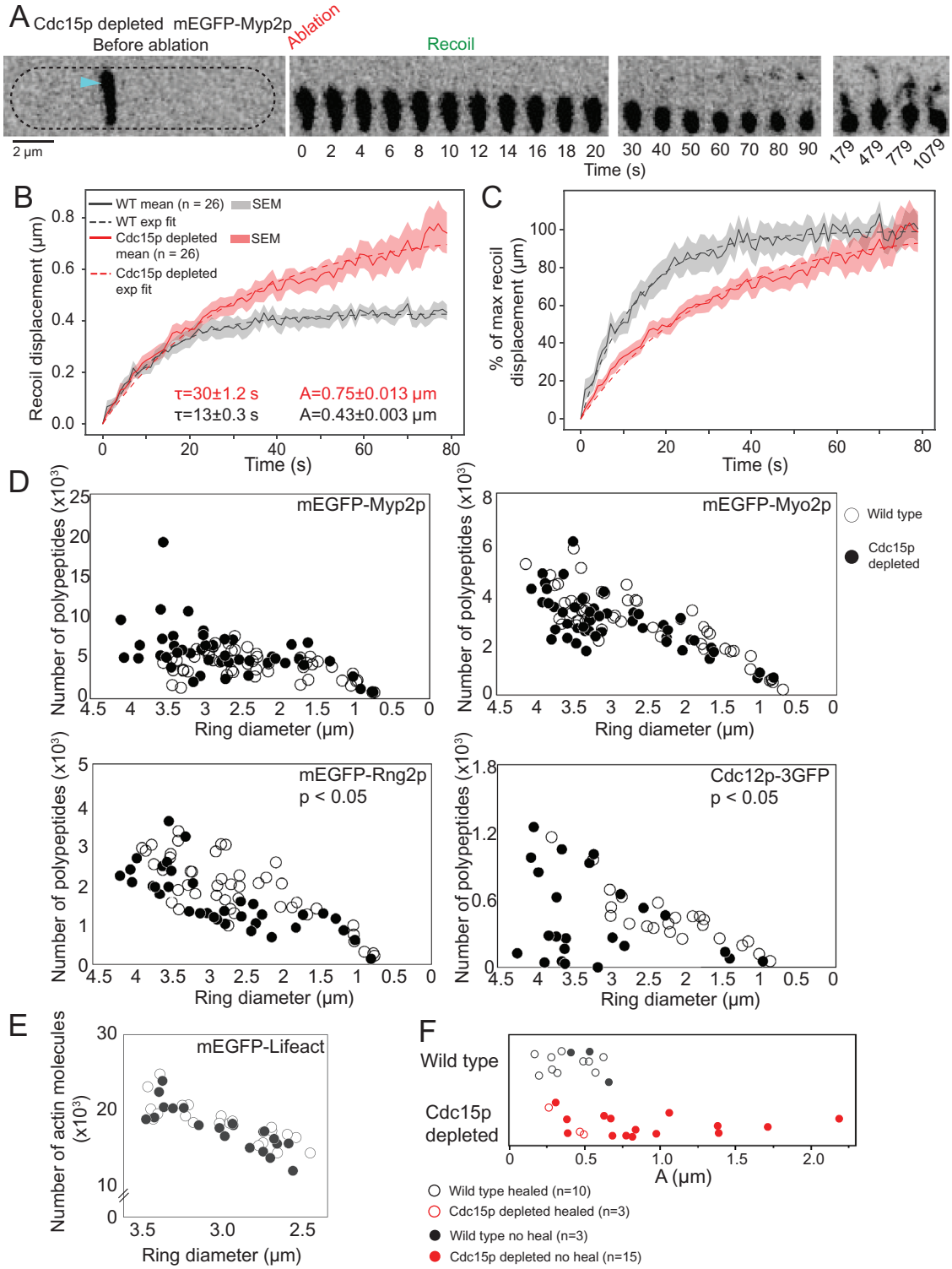

FIGURE 3: Ablated contractile rings in Cdc15p-depleted cells exhibit extended recoil and defective healing. (A) Left, single plane spinning disk confocal micrograph of a representative cell depleted of Cdc15p (dashed line outlines the cell) expressing mEGFP-Myp2p to visualize the contractile ring before ablation (targeted at cyan arrowhead). Right, cropped frames showing phases of the response to ablation. Contractile rings in cells depleted of Cdc15p do not consistently heal and constrict after ablation. Fluorescence, inverted grayscale. (B) Mean recoil displacement (solid line) ± standard error of the mean of all traces (SEM, shaded region) of 26 severed tips of ablated Cdc15p-depleted contractile rings (red) compared with wild type (black, data from Figure 1D). Exponential fit (dotted line) to this mean trace and its fit parameters (± the standard error on the least squares fit parameters) are listed. Time 0, first frame after ablation. (C) Mean recoil displacement data from (B), with each average trace rescaled as a percentage of the maximum average displacement to visualize the effect of changing τ. (D) Plots of the distribution of the number of polypeptides per ring for four cytokinesis proteins in wild-type and Cdc15p-depleted cells. Differences between the distribution of

Strains, growing conditions, and genetic and cellular methods

The *Schizosaccharomyces pombe* strains used in this study are listed in table S1. Strains were constructed by PCR-based gene targeting to integrate the constructs into the locus of choice and confirmed by PCR and fluorescence microscopy (Bahler *et al.*, 1998). For N-terminal tagging, the *pFA6a-kanMX6-Pcdc15-mEGFP* plasmid was constructed using ~800 bp of endogenous sequence upstream of the *cdc15* start codon. To generate a Cdc15p depletion strain, the *pFA6a-kanMX6-Pnmt81x-mCherry* plasmid was integrated at the endogenous locus of *cdc15* to replace its endogenous promoter with the repressible *Pnmt81x* promoter. Two repeats of GGA GGT were added to all insertions, creating a linker of four glycines between mEGFP or mCherry and the coding sequence of cdc15. The *Pnmt41x-HALO-Rho2CAAX* construct was cloned into pJK148 plasmid for integration into the *leu+* locus. The plasmids were verified by sequencing. For endogenous integration at the *cdc15* locus, primers with 80 bp of homologous sequence flanking the integration site (obtained at www.bahlerlab.info/resources/) were used to amplify the integration cassettes. All genomic integrations were confirmed by PCR and fluorescence microscopy.

For microscopy, cells were grown to exponential phase for 36–48 h in YE5S liquid medium in 50-mL baffled flasks at 25°C in a shaking incubator in the dark. To de-repress the expression of the *Pnmt41x-HALO-Rho2CAAX* plasma membrane marker construct, cells were shifted to EMM5S 16-18 h prior to imaging. To deplete the expression of Cdc15p, cells were grown for 24 h in YE5S and switched to YE5S + 15 μM thiamine for 16-18 h prior to imaging. Cells grown in liquid cultures were centrifuged at 2400 × *g* and washed in EMM5S (or EMM5S + 15 μM thiamine for depletion experiments) for imaging. Cells were concentrated 10- to 20-fold by centrifugation for 30 s at 2400 × *g*, washed in EMM5S (or EMM5S + 15 μM thiamine for depletion experiments), resuspended in EMM5S (or EMM5S + 15 μM thiamine for depletion experiments) and placed onto a thin disk of 25% porcine gelatin (Sigma-Aldrich; G-2500) dissolved in EMM5S (or EMM5S + 15 μM thiamine for depletion experiments). Cells were covered with a #1.5 coverslip, sealed with VALAP (1:1:1 Vaseline:lanolin:paraffin), and immediately imaged at room temperature (22°C).

Cells expressing *Pnmt41x-HALO-Rho2CAAX* were stained with 250 nM of JF635-HALO dye (gift from Luke Laevis, Janelia Labs) for 1 h in a shaking incubator at 25°C. Cells were pelleted as described above. The supernatant was removed, and the pellet was rinsed three times with EMM5S medium. The cells were then washed three times for 30–60 min each time with EMM5S in a shaking incubator. Cells were then pelleted and mounted for imaging as described above. This protocol was optimized for consistent labeling of HALO constructs in wild-type fission yeast cells. Using this protocol, we were able to achieve dependable labeling of the plasma membrane in most wild-type cells. Because expression of the HALO-Rho-2CAAX construct was driven by a *Pnmt41* repressible promoter, there was some variability in the level of fluorescent intensity in labeled cells.

Spinning disk microscopy and laser ablation

Data used for Supplemental Figure 2 and Figure 3, D and E were imaged using Nikon Eclipse Ti microscope equipped with a 100x/numerical aperture (NA) 1.49 HP Apo TIRF objective (Nikon), a CSU-X1 (Yokogawa) confocal spinning-disk system, 488/561 nm solid state lasers, and an electron-multiplying cooled charge-coupled device camera (EMCCD IXon 897, Andor Technology) (Cellular and Molecular Imaging Facility, CMIF). The Nikon Element software was used for acquisition.

For measurements of constriction rate, z-stacks of 19 optical planes across a total thickness of 6.48 μm through live fission yeast cells were acquired every minute for 2 h. For measuring protein concentration, a single z-stack of 21 optical planes across a total thickness of 6.48 μm through live fission yeast cells was acquired.

Data used for Figures 1, 3, A–C, F, Supplemental Figure 1, B, C, and F, Supplemental Figures 3 and 4 were imaged using a Nikon Ti-E microscope equipped with on an Andor Dragonfly spinning disk confocal fluorescence microscope equipped with 100x NA 1.45 objective (Nikon) and a built-in 1.5x magnifier; 488 nm diode laser with Borealis attachment (Andor); emission filter Chroma ET525/50m; and an EMCCD camera (iXon3, Andor Technology). Fusion software (Andor) was used to control data acquisition.

Targeted laser ablation was performed on constricting contractile rings in wild-type and Cdc15p-depleted cells expressing mEGFP-Myp2p using a MicroPoint (Andor) system with galvo-controlled steering to deliver 20-30 3 ns pulses of 551 nm light at 16-20 Hz (Andor) mounted on the Dragonfly microscope described above, as previously described (Zareiesfandabadi and Elting, 2022). Fusion software (Andor) was used to control acquisition while IQ software (Andor) was used simultaneously to control laser ablation. At this pulse rate, the ablation process lasts ~2 s. Chroma ET610LP mounted in the dichroic position of a Nikon filter turret was used to deliver the ablation laser to the sample. Since this filter also reflects the mEGFP emission, the camera frames collected during the ablation process are blank. The behavior of severed contractile rings was imaged immediately following laser ablation by acquiring a single confocal plane in the 488-nm channel every second for up to 5 min. The mechanism of ablative photodecomposition remains unclear but may be caused by either the propagation of a pressure wave and/or cavitation bubble dynamics (Venugopalan *et al.*, 2002; Rau *et al.*, 2006). The size of the damage is approximately the size of the diffraction spot of the lens <0.4 μm in XY plane and <0.8 in the Z axis (Khodjakov *et al.*, 1997).

We ablated 26 contractile rings in wild-type cells and 24 contractile rings in Cdc15p-depleted cells. This resulted in 26 severed tips that could be analyzed for the recoil phase of wild-type cells and 26 severed tips in Cdc15p-depleted cells. Of the ablated cells, 13 wild-type rings and 18 Cdc15p-depleted rings could be analyzed for a full 5 min. The reason the other contractile rings could not be analyzed were extensive photobleaching and drift in the z-position during the acquisition.

Serial ablation experiments were performed by continuously acquiring at 1 Hz, manually scanning the thickness of the cell

polypeptides was determined by a Kolmogorov–Smirnov test; $p < 0.05$ (stated on plots showing statistical difference). (E) Plots of the distribution of the number of actin molecules in the contractile rings of wild-type and Cdc15p-depleted cells based on quantitative measurements of *Pcof1-megfp-lifeact*. Differences between the distribution of molecules was determined by a Kolmogorov–Smirnov test, which was not significant based on $p < 0.05$. (F) Plot showing the relationship between the recoil magnitude A for each wild-type (same as in Supplemental Figure 1C) and Cdc15p-depleted ablated contractile ring and whether the respective contractile ring healed.

(automatic z-stack acquisition is not feasible with this setup), repositioning the focal plane to the surface of the contractile ring and ablating the ring as described above. The ablated contractile ring was re-ablated just before healing was complete for a total of 2-3 ablations (ablating 4 times or more resulted in cell death). Finally, the contractile ring thickness was manually scanned one final time. The constriction rate was measured by calculating the change in ring circumference from its diameter before and after serial ablation. Neighboring non-ablated cells were used as control.

Image analysis

ImageJ (Schneider *et al.*, 2012) and/or Nikon Elements were used to create maximum intensity projections of images, montages, and other image analyses. Except for time-lapse micrographs acquired after laser ablation, images in the figures are maximum intensity projections of z-sections spaced at 0.36 µm. Images were systematically contrasted to provide the best visualization, and images within the same figure panel were contrasted using the same settings. Confocal fluorescence micrographs in the figures are shown as inverted grayscale. Ring constriction rate was measured using kymographs of maximum projection images (19 z-confocal planes taken for 6.48 µm) of time-lapse datasets taken at 1-min time intervals. The kymographs were thresholded, the diameter of the projected ring was measured, and the circumference was calculated automatically as a function of this diameter for each time point. These values were plotted in Microsoft Excel and the constriction rate calculated using a linear regression to the constriction phase. Student's t-tests were used to determine whether constriction rates differed significantly between strains.

To count proteins in contractile rings, projection images of fields of cells were created from stacks of 21 optical images separated by 0.36 µm (Wu and Pollard, 2005; Wu *et al.*, 2008). The images were corrected for the camera noise and uneven illumination, and then the fluorescence intensity of contractile rings was measured. These fluorescence intensity measurements were compared against a standard curve of proteins tagged endogenously with mEGFP to determine the number of molecules per contractile ring (Wu and Pollard, 2005; Wu *et al.*, 2008). To count the number of actin monomers in the contractile ring, cells expressing *Pcof1-mEGFP-Lifeact* were imaged (Malla *et al.*, 2021). The fluorescence intensity of contractile rings corresponding to the size of those ablated (~2.5–3.5 µm diameter corresponding to 50-80% of their initial size) was measured. These fluorescence intensity measurements were compared against a standard curve of proteins tagged endogenously with monomeric EGFP (mEGFP) to determine the number of molecules per contractile ring (Wu and Pollard, 2005; Wu *et al.*, 2008). The resulting actin monomer values were then scaled appropriately to reflect that this Lifeact construct marks 6% of polymerized actin (Malla *et al.*, 2021). Two-sample Kolmogorov–Smirnov (KS) tests were used to determine whether the distribution of polypeptides in the constricting contractile ring differed between wild-type and Cdc15p-depleted cells. The null hypothesis was that the samples are drawn from the same distribution of polypeptides. The cumulative distribution functions (CDFs) for polypeptide number were calculated for each of the markers and genetic backgrounds, and the maximum difference between pairs of CDFs was calculated and compared with the KS test critical value at a significance level of $p < 0.05$. If the maximum difference between the CDFs was greater than the critical value, the null hypothesis was rejected.

To understand the relative level of Cdc15p remaining in cells with the *Pnmt81-mEGFP-cdc15* construct after either repression or depletion when compared with the endogenous concentration, sum projection images of fields of cells were created from stacks of 19 optical images separated by 0.36 µm. Cells were stained with Fluorescent Brightener 28 to determine the extent of ring constriction. Using FIJI, we measured the fluorescence intensity of contractile rings that had just begun to constrict. The contractile ring fluorescence intensity values were normalized for the fluorescence intensity of the cytoplasmic noise of each cell. The normalized fluorescence intensity values of the derepressed and depleted cells were then divided by the normalized fluorescence intensity values of the endogenous mEGFP-Cdc15p cells.

The percentage offset of the septum was measured using maximum intensity projection images of still micrographs of cells expressing mEGFP-Myo2p and stained with calcofluor to highlight the cell wall. The center of the cell was calculated as half of the cell length. The position of constricting contractile rings in cells showing a septum by calcofluor staining was measured as the distance of the contractile ring from the cell tip. The percentage offset was calculated as the distance between the position of the contractile ring and the calculated cell center over half of the cell length.

The displacement of the tips of severed contractile rings was tracked manually every second after laser ablation using the "multi-point" tool in FIJI on single z-plane time-lapse micrographs. The severed tips were tracked until they recoiled out of the imaging plane or until the contractile ring was healed. The coordinates of the tracked severed tips were exported as a CSV file. The displacement of the severed tips starting from the first frame after severing, t = 0 s, was calculated from the coordinates of the tracked severed tips using custom Python codes. The displacement traces from each cell were aligned to t = 0 s and the mean displacement curve was calculated for each genotype. The displacement traces show the combined recoil phase of all severed tips exclusively. The recoil displacement of each the severed tips contributes to the traces until the recoil halts. The mean displacement curve for each genotype was fit to a single exponential $\Delta L(t) = A\left(1 - e^{-\frac{t}{\tau}}\right)$ using a least squares fit, and the standard error on the least squares fit is reported. Contractile rings were considered fully ablated if there was no remaining fluorescence joining the ablated tips of the ring and the ablated ends showed evidence of recoil away from the site of ablation. Fully ablated rings also healed by the ablated tips slowly growing back towards each other, while the healing of partially ablated rings occurred as a uniform fluorescence recovery across the gap. This also resulted in the healing duration of partially ablated rings being much faster than fully ablated rings.

Changes in fluorescence intensity after laser ablation were calculated from single optical plane time-lapse micrographs of severed contractile rings. Images were corrected for photobleaching using the "exponential method" in FIJI when photobleaching was detected over the duration of analysis. A region of interest (ROI) of size 5 µm x 1 µm containing the entire ring was selected using the "line tool" in FIJI. The mean fluorescence for each line of pixels perpendicular to the length of the contractile ring was measured at each time point. The mean fluorescence intensity of the cytoplasmic background was measured at each time point in a circular ROI of 1 µm in diameter at a position away from the ring. The fluorescence from the cytoplasmic background was subtracted from the fluorescent intensity of the contractile ring at each time point, giving us a trace of background subtracted intensity over time. These background-subtracted intensities were used to create kymographs with custom Python codes. For each kymograph, the range of fluorescence intensities were

set so the highest pixel value is 1 and the lowest pixel value is zero.

The maximum value of the peak over time, normalized to its intensity prior to ablation, was calculated by identifying the pixel with maximum intensity at each time point in the background subtracted kymograph described above. Then, this 1-D intensity trace was normalized to the average maximum intensity value for the 10 frames prior to ablation. The means (as a function of time) of all of these normalized traces under each cellular condition were then calculated.

To calculate the normalized total fluorescence, total fluorescence along each column of pixels of the kymograph was calculated by integrating the total fluorescent intensity of mEGFP-Myp2p within that column, yielding a single intensity vs. time trace for each movie. Each trace was normalized by dividing it by the average intensity of the 5 frames prior to ablation, and the mean of all traces under each condition were calculated. Standard error of the mean was calculated at each timepoint.

ACKNOWLEDGMENTS

We thank Julio Belmonte, Julien Berro, Brié Levesque and Thomas D. Pollard for useful comments. We thank Mamata Malla and Qian Chen for sharing their *Pcof1-mEGFP-Lifeact* strain. We thank the CMIF at NCSU (supported by the State of North Carolina and NSF) for the ablation microscope. This work was funded by NIH R01GM134254 and NIH R35GM138083.

REFERENCES

Angers-Loustau A, Cote JF, Charest A, Dowbenko D, Spencer S, Lasky LA, Tremblay ML (1999). Protein tyrosine phosphatase-PEST regulates focal adhesion disassembly, migration, and cytokinesis in fibroblasts. J Cell Biol 144, 1019–1031.

Arasada R, Pollard TD (2014). Contractile ring stability in S. pombe depends on F-BAR protein Cdc15p and Bgs1p transport from the Golgi complex. Cell Rep 8, 1533–1544.

Arasada R, Pollard TD (2015). A role for F-BAR protein Rga7p during cytokinesis in S. pombe. J Cell Sci 128, 2259–2268.

Atilgan E, Magidson V, Khodjakov A, Chang F (2015). Morphogenesis of the Fission Yeast Cell through Cell Wall Expansion. Curr Biol 25, 2150–2157.

Bahler J, Wu JQ, Longtine MS, Shah NG, McKenzie A 3rd, Steever AB, Wach A, Philippsen P, Pringle JR (1998). Heterologous modules for efficient and versatile PCR-based gene targeting in Schizosaccharomyces pombe. Yeast 14, 943–951.

Bellingham-Johnstun K, Anders EC, Ravi J, Bruinsma C, Laplante C (2021). Molecular organization of cytokinesis node predicts the constriction rate of the contractile ring. J Cell Biol 220.

Carnahan RH, Gould KL (2003). The PCH family protein, Cdc15p, recruits two F-actin nucleation pathways to coordinate cytokinetic actin ring formation in Schizosaccharomyces pombe. J Cell Biol 162, 851–862.

Colombelli J, Besser A, Kress H, Reynaud EG, Girard P, Caussinus E, Haselmann U, Small JV, Schwarz US, Stelzer EH (2009). Mechanosensing in actin stress fibers revealed by a close correlation between force and protein localization. J Cell Sci 122, 1665–1679.

Kassianidou E, Brand CA, Schwarz US, Kumar S (2017). Geometry and network connectivity govern the mechanics of stress fibers. Proc Natl Acad Sci USA 114, 2622–2627.

Khodjakov A, Cole RW, Rieder CL (1997). A synergy of technologies: combining laser microsurgery with green fluorescent protein tagging. Cell Motil Cytoskeleton 38, 311–317.

Kumar S, Maxwell IZ, Heisterkamp A, Polte TR, Lele TP, Salanga M, Mazur E, Ingber DE (2006). Viscoelastic retraction of single living stress fibers and its impact on cell shape, cytoskeletal organization, and extracellular matrix mechanics. Biophys J 90, 3762–3773.

Laplante C, Berro J, Karatekin E, Hernandez-Leyva A, Lee R, Pollard TD (2015). Three myosins contribute uniquely to the assembly and constriction of the fission yeast cytokinetic contractile ring. Curr Biol 25, 1955–1965.

Laplante C, Huang F, Tebbs IR, Bewersdorf J, Pollard TD (2016). Molecular organization of cytokinesis nodes and contractile rings by super-resolution fluorescence microscopy of live fission yeast. Proc Natl Acad Sci USA 113, E5876–E5885.

Laporte D, Coffman VC, Lee IJ, Wu JQ (2011). Assembly and architecture of precursor nodes during fission yeast cytokinesis. J Cell Biol 192, 1005–1021.

Lord M, Pollard TD (2004). UCS protein Rng3p activates actin filament gliding by fission yeast myosin-II. J Cell Biol 167, 315–325.

Malla M, Pollard TD, Chen Q (2021). Counting actin in contractile rings reveals novel contributions of cofilin and type II myosins to fission yeast cytokinesis. Mol Biol Cell, mbcE21080376.

McDargh Z, Wang S, Chin HF, Thiyagarajan S, Karatekin E, Pollard TD, O'Shaughnessy B (2021). Myosins generate contractile force and maintain organization in the cytokinetic contractile ring. bioRxiv, 2021.2005.2002.442363.

McDonald NA, Lind AL, Smith SE, Li R, Gould KL (2017). Nanoscale architecture of the Schizosaccharomyces pombe contractile ring. eLife 6, e28865.

McDonald NA, Vander Kooi CW, Ohi MD, Gould KL (2015). Oligomerization but Not Membrane Bending Underlies the Function of Certain F-BAR Proteins in Cell Motility and Cytokinesis. Dev Cell 35, 725–736.

Mishra M, Kashiwazaki J, Takagi T, Srinivasan R, Huang Y, Balasubramanian MK, Mabuchi I (2013). In vitro contraction of cytokinetic ring depends on myosin II but not on actin dynamics. Nat Cell Biol 15, 853–859.

Morita R, Numata O, Nakano K, Takaine M (2021). Cell cycle-dependent phosphorylation of IQGAP is involved in assembly and stability of the contractile ring in fission yeast. Biochem Biophys Res Commun 534, 1026–1032.

Oh Y, Schreiter J, Nishihama R, Wloka C, Bi E (2013). Targeting and functional mechanisms of the cytokinesis-related F-BAR protein Hof1 during the cell cycle. Mol Biol Cell 24, 1305–1320.

Rau KR, Quinto-Su PA, Hellman AN, Venugopalan V (2006). Pulsed laser microbeam-induced cell lysis: time-resolved imaging and analysis of hydrodynamic effects. Biophys J 91, 317–329.

Roca-Cusachs P, Conte V, Trepat X (2017). Quantifying forces in cell biology. Nat Cell Biol 19, 742–751.

Russell RJ, Xia SL, Dickinson RB, Lele TP (2009). Sarcomere mechanics in capillary endothelial cells. Biophys J 97, 1578–1585.

Schneider CA, Rasband WS, Eliceiri KW (2012). NIH Image to ImageJ: 25 years of image analysis. Nat Methods 9, 671–675.

Silva AM, Osorio DS, Pereira AJ, Maiato H, Pinto IM, Rubinstein B, Gassmann R, Telley IA, Carvalho AX (2016). Robust gap repair in the contractile ring ensures timely completion of cytokinesis. J Cell Biol 215, 789–799.

Snider CE, Willet AH, Chen JS, Arpag G, Zanic M, Gould KL (2017). Phosphoinositide-mediated ring anchoring resists perpendicular forces to promote medial cytokinesis. J Cell Biol 216, 3041–3050.

Spencer S, Dowbenko D, Cheng J, Li W, Brush J, Utzig S, Simanis V, Lasky LA (1997). PSTPIP: a tyrosine phosphorylated cleavage furrow-associated protein that is a substrate for a PEST tyrosine phosphatase. J Cell Biol 138, 845–860.

Spira F, Cuylen-Haering S, Mehta S, Samwer M, Reversat A, Verma A, Oldenbourg R, Sixt M, Gerlich DW (2017). Cytokinesis in vertebrate cells initiates by contraction of an equatorial actomyosin network composed of randomly oriented filaments. eLife 6, e30867.

Swulius MT, Nguyen LT, Ladinsky MS, Ortega DR, Aich S, Mishra M, Jensen GJ (2018). Structure of the fission yeast actomyosin ring during constriction. Proc Natl Acad Sci USA 115, E1455–E1464.

Tebbs IR, Pollard TD (2013). Separate roles of IQGAP Rng2p in forming and constricting the Schizosaccharomyces pombe cytokinetic contractile ring. Mol Biol Cell 24, 1904–1917.

Vavylonis D, Wu JQ, Hao S, O'Shaughnessy B, Pollard TD (2008). Assembly mechanism of the contractile ring for cytokinesis by fission yeast. Science 319, 97–100.

Venugopalan V, Guerra A 3rd, Nahen K, Vogel A (2002). Role of laser-induced plasma formation in pulsed cellular microsurgery and micromanipulation. Phys Rev Lett 88, 078103.

Wang S, O'Shaughnessy B (2019). Anchoring of actin to the plasma membrane enables tension production in the fission yeast cytokinetic ring. Mol Biol Cell 30, 2053–2064.

Willet AH, Bohnert KA, Gould KL (2018). Cdk1-dependent phosphoinhibition of a formin-F-BAR interaction opposes cytokinetic contractile ring formation. Mol Biol Cell 29, 713–721.

Willet AH, Igarashi MG, Chen JS, Bhattacharjee R, Ren L, Cullati SN, Elmore ZC, Roberts-Galbraith RH, Johnson AE, Beckley JR, Gould KL (2021). Phosphorylation in the intrinsically disordered region of F-BAR protein Imp2 regulates its contractile ring recruitment. J Cell Sci 134, 258645.

Wollrab V, Thiagarajan R, Wald A, Kruse K, Riveline D (2016). Still and rotating myosin clusters determine cytokinetic ring constriction. Nat Commun 7, 11860.

Wu JQ, Kuhn JR, Kovar DR, Pollard TD (2003). Spatial and temporal pathway for assembly and constriction of the contractile ring in fission yeast cytokinesis. Dev Cell 5, 723–734.

Wu JQ, McCormick CD, Pollard TD (2008). Chapter 9: Counting proteins in living cells by quantitative fluorescence microscopy with internal standards. Methods Cell Biol 89, 253–273.

Wu JQ, Pollard TD (2005). Counting cytokinesis proteins globally and locally in fission yeast. Science 310, 310–314.

Wu JQ, Sirotkin V, Kovar DR, Lord M, Beltzner CC, Kuhn JR, Pollard TD (2006). Assembly of the cytokinetic contractile ring from a broad band of nodes in fission yeast. J Cell Biol 174, 391–402.

Zareiesfandabadi P, Elting MW (2022). Force by minus-end motors Dhc1 and Klp2 collapses the S. pombe spindle after laser ablation. Biophys J 121, 263–276.